AGU PUBLICATIONS

JGR

Journal of Geophysical Research: Solid Earth

RESEARCH ARTICLE
10.1002/2013JB010834

Key Points:
- Landward vergence suggests localized weak plate boundary interface
- Major fault evolution model based on fault plane character
- Complex accretionary prism structure driven by downgoing plate features

Correspondence to:
B. J. Cook,
b.cook@noc.soton.ac.uk

Citation:
Cook, B. J., T. J. Henstock, L. C. McNeill, and J. M. Bull (2014), Controls on spatial and temporal evolution of prism faulting and relationships to plate boundary slip offshore north-central Sumatra, *J. Geophys. Res. Solid Earth*, *119*, 5594–5612, doi:10.1002/2013JB010834.

Received 11 NOV 2013
Accepted 9 JUN 2014
Accepted article online 12 JUN 2014
Published online 10 JUL 2014

Controls on spatial and temporal evolution of prism faulting and relationships to plate boundary slip offshore north-central Sumatra

Becky J. Cook[1], Timothy J. Henstock[1], Lisa C. McNeill[1], and Jonathan M. Bull[1]

[1]Ocean and Earth Science, National Oceanography Centre Southampton, University of Southampton, Southampton, UK

Abstract Across- and along-strike variations in the morphology and structure of the north-central Sumatran forearc (~1.5°S to 1°N) are broadly coincident with subducting plate topography and an earthquake segment boundary zone below the Batu Islands. We present a detailed interpretation of multichannel streamer seismic reflection data collected offshore north-central Sumatra, to better characterize the morphological and structural variations, provide insight into fault development, and relate structure to plate boundary rupture and seismicity patterns. We interpret two relatively continuous, major fault structures that divide the prism into three strike-parallel belts that can be characterized by the relative fault slip rates along major and minor fault structures. The midslope break fault(s) and upper slope-bounding fault(s) are major, potentially out-of-sequence thrusts accommodating a significant component of the compressional strain. We propose that the upper slope-bounding fault represents the more mature end-member of an evolving fault system. Landward vergent structures are associated with a relatively thin sedimentary section near the deformation front in the center of our study area and suggest a potentially weak shallow plate boundary associated with the subducting Wharton Fossil Ridge.

1. Introduction

The Sumatra-Andaman margin is composed of a series of earthquake rupture zones and segment boundaries exhibiting variable slip characteristics. The modern records of ruptures spanning 2004–2010, along with historical accounts and paleogeodetic (coral uplift) data, have allowed scientists to define three major segments of the margin (Figure 1). The M_w 9.2 December 2004 earthquake ruptured the ~1300 km long north Sumatra-Andaman segment, which exhibits internal variability in rupture speed and the potential for shallow earthquake slip [*Lay et al.*, 2005]. In the Nias segment, which ruptured during the M_w 8.7 March 2005 and historic 1861 earthquakes, the shallow megathrust slips aseismically, and earthquake slip is concentrated below the outer forearc high [*Hsu et al.*, 2006]. The Mentawai segment, extending from the Batu Islands to Enggano Island, ruptured completely in 1833, but more recently in smaller, sometimes tsunamigenic earthquake ruptures [*Bilek et al.*, 2011; *Natawidjaja et al.*, 2004; *Natawidjaja et al.*, 2006; *Newcomb and McCann*, 1987].

Margin-scale geophysical studies have constrained variations in overall prism morphology and structure of the Sunda subduction zone and have noted along-strike changes in seafloor prism profiles and vergence sense among the different segments [*Kopp et al.*, 2008; *McNeill and Henstock*, 2014; *Moeremans et al.*, 2014; *Moore et al.*, 1980], but a detailed comparison of the structure and seismicity is lacking, particularly for the margin offshore north-central Sumatra. In addition, although detailed studies interpreting dense 2-D seismic reflection data covering several hundreds of kilometers are relatively uncommon, those that are available show that prism structure can change rapidly along strike [e.g., *MacKay et al.*, 1992; *Smith et al.*, 2012].

Here we present a detailed interpretation of multichannel seismic (MCS) data to provide insight into the development and evolution of the outer forearc accretionary prism structure and morphology. We focus on ~10–100 km scale along- and across-strike variations in structure observed across the segment boundary separating the Nias and Mentawai segments. We define the Batu Segment Boundary Zone as the low coupling region below the Batu Islands identified by *Chlieh et al.* [2008], and we compare the observed changes in the structure and morphology to earthquake slip, coupling models, and locally recorded aftershocks to highlight possible relationships between structure and seismicity.

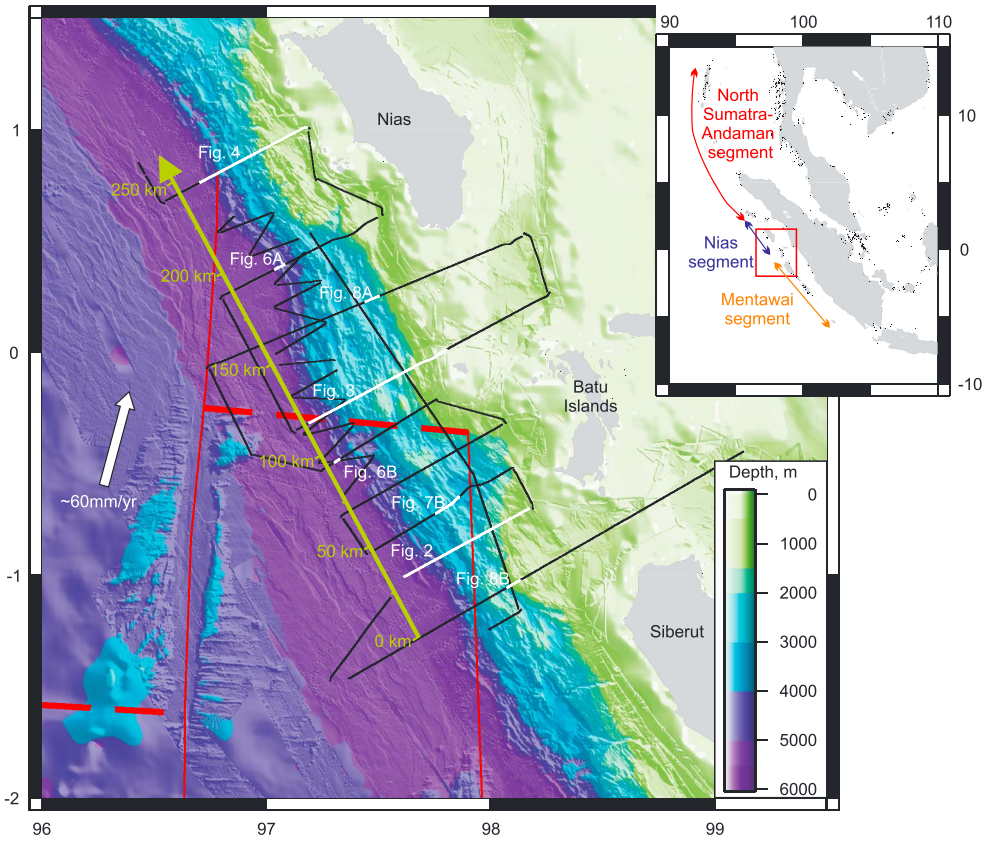

Figure 1. Bathymetric map of study area showing Australian-Sundaland relative plate motion (white arrow), the incoming Wharton Fossil Ridge (dashed red lines) and associated fracture zones (solid red lines), all MCS seismic lines (black) and MCS lines shown in Figures 2–4 and 6–8 (white). Inset: regional map with the three major segments of the Sunda subduction zone.

1.1. Background

Megathrust earthquake nucleation is often concentrated below the forearc basin, and the outer forearc high typically marks the transition from an updip aseismic zone (outer wedge) into the seismogenic inner wedge [e.g., *Byrne et al.*, 1988; *Wang and Hu*, 2006; *Wells et al.*, 2003]. Weak, unconsolidated sediments of the outer wedge undergo internal deformation, and the weak (steady state, low velocity), presumably velocity-strengthening underlying plate boundary is thought to be unable to accumulate the necessary stress required for earthquake rupture initiation [*Marone and Saffer*, 2007; *Scholz*, 1998]. However, coseismic rupture can potentially propagate into the outer wedge following a deeper rupture if enough energy is released to overcome the fracture energy [*Kanamori*, 2001], which can lead to runaway slip if the outer wedge material is also velocity weakening [*Faulkner et al.*, 2011; *Ide et al.*, 2011; *Ujiie et al.*, 2013]. Conversely, the material comprising the inner wedge and underlying plate boundary is stronger resulting from near complete compaction and dewatering of sediments or the presence of a continental backstop and identified by a stable taper angle and deforms in elastic-brittle (stick-slip) cycles [e.g., *Byrne et al.*, 1988; *Fuller et al.*, 2006; *Moore et al.*, 2007].

The outer wedge structure at accretionary margins typically comprises a sequence of seaward propagating and vergent imbricate thrust sheets [e.g., *Moore et al.*, 2009; *Smith et al.*, 2012]. Some margins deviate from this model and are characterized by mixed or landward vergence and/or more complex faulting/deformation patterns [e.g., *Gulick et al.*, 1998; *Moore et al.*, 1980; *Seely*, 1977]. At the outer-arc high, the structural style changes and minimal internal deformation occurs within the older prism underlying the forearc basin. This change in deformation style is commonly coincident with the inner/outer wedge transition and the plate boundary underlying the forearc basin considered seismogenic [e.g., *Byrne et al.*, 1988].

Seaward dipping thrusts (and related landward vergent folds) are relatively uncommon globally but are observed in parts of several prisms, including offshore Washington-Oregon-northern California (Cascadia), northern Panama, southern Chile, and Sumatra, and in fossil prisms in Alaska and Japan [*Gulick et al.*, 1998; *Henstock et al.*, 2006; *MacKay et al.*, 1992; *McNeill and Henstock*, 2014; *Moeremans et al.*, 2014; *Polonia and Torelli*, 2007; *Reed et al.*, 1990; *Seely*, 1977]. The development of landward vergent structures at the prism toe is not well understood, but low basal shear stress is a commonly cited prerequisite [*Gutscher et al.*, 2001; *MacKay et al.*, 1992; *Seely*, 1977], and sandbox models with varied basal friction highlight increased backthrust deformation and symmetry of structures in models with decreased basal friction [*Huiqi et al.*, 1992].

Out-of-sequence thrusts (OOST) are commonly found near and contribute to uplift of the outer forearc high [e.g., *Barnes et al.*, 2002; *Gulick et al.*, 2010]. Others are observed in a midslope position and may indicate a dynamic backstop composed of lithified, accreted sediments [*Kopp and Kukowski*, 2003]. OOST are often associated with negative polarity reflections [e.g., *Bangs et al.*, 2009; *Collot et al.*, 2008] and are thought to be important conduits for fluid flow within accretionary prisms [*Saffer and Tobin*, 2011]. Coseismic slip along major OOST (or megasplay faults) may be an important mechanism in tsunami generation [e.g., *Park et al.*, 2002].

Along-strike changes in coupling are thought to be responsible for lack of (fast) seismic rupture at some subduction margins and varied slip behavior at others [e.g., *Chlieh et al.*, 2008; *Scholz and Campos*, 2012]. Gaps in the seismic record can be grouped into two categories: (1) areas that are well coupled with a significant future rupture potential and are considered "gaps" due to the limited earthquake record [e.g., *Loveless and Meade*, 2011; *Smith et al.*, 2013] and (2) areas where decreased effective friction along the plate boundary (i.e., a weakened plate boundary) promotes aseismic or slow slip events [e.g., *Bell et al.*, 2010; *Chlieh et al.*, 2008].

Decreased effective friction along the subduction plate boundary is often associated with excess fluid pressures, which lower the effective normal stress [e.g., *Davis et al.*, 1983]. Increased fluid pressures outboard of the deformation front, in protodécollement horizons, may build up where sedimentation rates are high and rapid burial traps fluids; thick sediments and increased temperatures lead to early dewatering reactions; or where continuous recharge by deeper fluids is occurring [*Bangs et al.*, 1999; *Geersen et al.*, 2013]. Landward of the deformation front, high fluid pressures develop as a result of dewatering and compaction reactions and/or underthrusting of fluid-rich, undercompacted sediments [*Bangs et al.*, 2009; *Moore et al.*, 2001; *Saffer and Tobin*, 2011]. Fluid-rich zones capped by low-porosity sedimentary horizons or faults are often recognized on seismic reflection profiles as negative polarity reflectors and have been drilled and sampled at the Barbados [*Bangs et al.*, 1999], Cascadia [*Moore et al.*, 1995], and Nankai margins [*Moore and Shipley*, 1993].

1.2. Regional Geologic Setting

At the Sunda subduction zone, the Australian-Indian Plate is being obliquely subducted beneath the Sundaland Plate at a rate of ~60 mm/yr [*DeMets et al.*, 2010]. Earthquake slip along the north-central Sumatran subduction plate boundary is dominantly dip-slip, suggesting that plate motion is partitioned into nearly perpendicular convergence accommodated across the trench and strike-slip motion along the Great Sumatran Fault and the other strike-slip faults in the forearc [*Bock et al.*, 2003; *Fitch*, 1972; *McCaffrey et al.*, 2000]. The perpendicular component of convergence varies from ~40–45 mm/yr offshore central Sumatra to ~20 mm/yr offshore of the Andaman Islands in the north [*McCaffrey*, 2009; *McNeill and Henstock*, 2014].

Offshore north-central Sumatra, the youngest oceanic plate, approximately 45 Ma, is found at E-W trending segments of the Wharton Fossil Ridge (WFR); plate age increases north and south of the ridge to approximately 70 Ma offshore of the Nicobar Islands [*Liu et al.*, 1983]. The WFR is recognized as broad high in the oceanic basement topography and is offset by highs associated with N-S trending fracture zones (FZs) at ~98°E (the Investigator Fracture Zone (IFZ)) and at 96.5°E in our study area (Figure 1). Previous studies of the Sumatran margin have noted apparent correlations between the patterns of plate boundary seismicity and coupling, subducting plate structures, and seafloor morphology, suggesting that there may be a relationship between the rupture behavior and the subducting plate structure in this area [*Chlieh et al.*, 2008; *Lange et al.*, 2010].

The incoming plate sedimentary sequence is composed of prefan pelagic and Bengal-Nicobar fan sediments overlain by trench wedge deposits [*Moore and Curray*, 1980]. The thickness of sediments on the incoming plate is regionally controlled by proximity to the Bengal-Nicobar fan source and locally by oceanic basement

Table 1. Summary of the Different Processing Flows Applied to MCS Seismic Lines Interpreted in This Study

Processing Steps	SUMD Lines	SUMD03
Band-pass filter	3-5-50-62.5	3-5-50-80
Predictive decon	Y	Y
F-K filter	Y	Y
Multiple removal	N	Y
Velocity analysis	Y	with dip-moveout correction
Prestack time migration	Y	Y
Postmigration stack	Y	Y
Top mute	Y	Y
F-K filter	N	Y
Automatic gain control (1000 m/s)	Y	Y

topography. Sediment thickness at the trench varies from ~1–3 km near the Batu Segment Boundary Zone to >4 km northwest of Sumatra [*Dean et al.*, 2010; *Geersen et al.*, 2013; *Gulick et al.*, 2011; *McNeill and Henstock*, 2014].

In the north Sumatra-Andaman segment, the outer forearc is typically characterized by a relatively narrow and steep outermost slope which transitions to a broad plateau farther arcward [*Cochran*, 2010; *McNeill and Henstock*, 2014; *Moore et al.*, 1980]. Landward verging folds and seaward dipping faults are relatively common at the prism toe [*Henstock et al.*, 2006; *McNeill and Henstock*, 2014; *Moeremans et al.*, 2014], and a strong negative polarity reflector, interpreted as a protodécollement surface, is observed in the thick (4.0–4.5 km) incoming sedimentary section [*Dean et al.*, 2010]. In the Nias segment, the prism width is narrow, with a steep outermost slope resulting from surface erosion [*Kopp et al.*, 2008]. Near the Batu Segment Boundary Zone, the outermost slope is variable, and the deformation front has an irregular trend due to the subduction of the WFR and IFZ [*Kopp et al.*, 2008]. In the Mentawai segment, the overall prism broadens and shallows relative to the Nias segment [*Kopp et al.*, 2008]; the downgoing plate is characterized by variable basement topography which commonly outcrops at the seafloor, and the mixed vergence structures are observed near the deformation front [*Singh et al.*, 2011].

2. Data Acquisition and Processing

Following the Sumatran megathrust earthquakes in December 2004 and March 2005, data were collected in an effort to understand the different rupture characteristics, the segmentation of the plate boundary, and the details of the forearc structure. Data pertinent to this study are swath bathymetric data collected on various cruises by UK- and German-funded studies and multichannel streamer (MCS) seismic data collected on board the UK-funded R/V *Sonne* in 2008 (cruise SO198) and 2009 (cruise SO200).

The swath bathymetric data were collected on board the R/V *Sonne* using a Simrad EM120, with a 1° beam width resulting in a minimum horizontal resolution of ~100 m near the trench. The swath bathymetric data were combined to produce a 0.002° × 0.002° grid and supplemented with General Bathymetric Chart of the Oceans bathymetry [*Smith and Sandwell*, 1997]. The resultant grid is shown with illumination from the SW in Figure 1.

MCS seismic data collected offshore central Sumatra during SO198 used a 88.8l (5420 in^3), 13.8MPa (2000psi) source, shot at 20 s (~50 m) intervals and a 192-channel, 2.4 km long fluid-filled digital streamer to record the data. The data are a series of dip sections, with line spacing of approximately 20–30 km, and adjoining strike lines covering ~250 km along strike between Siberut and Nias Islands (Figure 1). Data collected during SO200 used a smaller source 22.9l (1400 in^3) and a shorter streamer (24 channel, 300 m); they form a series of trench oblique profiles, with an average spacing of approximately 5 km and along-strike coverage of ~150 km (Figure 1).

All MCS data are shown as prestack time migrations with varying degrees of preprocessing (details shown in Table 1). The relatively short streamer and complex prism structure presents a challenge for imaging structures greater than ~2.0 m/s below the seafloor, and the interpretations presented are dotted on Figures 2–4 and 6–8, where they are uncertain. Our interpretation is based on combined observations from the data at various stages of processing including the common depth point reflection gathers, stacked sections, and prestack time-migrated sections. Where approximate depth values are given, they are based on a simple three-layer velocity model composed of a 1500 m/s water layer; a 1.0 km thick, upper sediment layer with interval velocity of 2000 m/s; and a lower sediment/rock layer with interval

velocity of 4000 m/s [*Kieckhefer et al.*, 1980]. Incoming sediment section thicknesses are calculated using an average sediment velocity of 2500 m/s, and slope sediment thicknesses are calculated using an average sediment velocity of 2000 m/s.

3. Results

In the following description, we have defined an along strike distance axis approximately parallel to the trench with the zero point located at ~1.5°S (Figure 1). The distances along individual seismic profiles are given as distance from the deformation front (DF) and are marked on all profiles. The accretionary prism is complexly faulted, and for ease of description, faults coincident with major bathymetric ridges were named numerically from the DF landward. Along strike equivalent faults have the same number but can be identified as a different fault by the alphabetical suffix. Faults appended with "a"s are the southernmost, and as new faults are identified along strike, they are named with the subsequent letter suffix, i.e., 1a, 1b, and 1c. The comprehensive interpretation of the outer forearc incorporates the analysis of all the profiles shown in Figure 1; three representative profiles are described in the following sections.

3.1. Incoming Plate Structure

The incoming plate has variable oceanic basement topography across the study area; the oceanic basement outcrops on the seafloor along ~N-S oriented FZs at ~96.5°E and 98°E (Figure 1). The sediment thickness on the incoming plate varies rapidly both along and across strike from no cover on the incoming FZs outboard of the trench to ~3 km in the deepest trench sections. At the deformation front, the thinnest sedimentary section (~1 km thick) is observed ~100 km along strike, where the WFR intersects the trench; here the outer prism bulges upward, and the deformation front steps seaward, producing a trench salient from ~80 to 160 km along strike (Figure 1). The thickest input sedimentary section (~3 km thick) is found between ~160 and 190 km along strike, in a trench reentrant north of the salient (Figure 1). Other more localized variations in sediment thickness are also controlled by the topography of the oceanic basement. There is no high-amplitude negative polarity reflector within the deepest sediments as observed offshore north Sumatra [*Dean et al.*, 2010; *Geersen et al.*, 2013]. Normal faults offsetting the incoming sediment section, observed on the bathymetric data outboard of the trench wedge, are largely trench parallel but are rotated to an ~N-S trend near FZs (Figure 1). These faults cut the entire section to the seafloor seaward of the trench wedge, whereas nearer to the deformation front, the faults are buried by trench wedge deposits.

3.2. SUMD03

Line SUMD03 is located in the south of our study area (~30 km along strike) and extends from 4 km seaward of the DF to 68 km landward into the outer forearc wedge. The incoming sedimentary section is ~2.0 km thick at the trench, and the top of the oceanic basement is imaged for ~45 km below the prism. The imaged wedge is cut by a series of landward dipping imbricate thrusts resulting in a series of bathymetric ridges with spacing of 6–11 km and numerous smaller thrusts with variable dip direction (Figure 2).

The outermost wedge (0–33 km from DF) is characterized by a rugose seafloor, which results in pull-up and out-of-plane reflections that obscure the subsurface structure and seafloor, respectively. The seafloor roughness reflects a combination of recent fault activity, limited slope sedimentation, and erosion. The frontal structure asymmetry and the bulk of compressional deformation accommodated across it are landward vergent, but there is no offset observed along any potential seaward dipping fault planes. Offset is observed along Fault 1a, which is landward dipping, has a negative polarity fault plane reflection, and soles into the top of oceanic basement. The fault planes of Faults 2a and 3a are poorly imaged, and we interpret the faults based on discontinuities in the sediment reflections. Sedimentary reflections also define hanging wall anticlines, which are deformed by minor faults and eroded at the surface. Fault 4a has a negative polarity fault plane reflection that shallows in dip and decreases in amplitude at depth (>~6 km). The Fault 4a hanging wall block is characterized by chaotic seismic character, and the locally steepest seafloor slope (23°) is coincident with seafloor collapse on the seaward edge (of the hanging wall block). Between 34 and 39 km from the deformation front, several kilometer-scale horse blocks are imaged below a thin cover of slope sediments (100–200 m vertical thickness), which suggests that the chaotic character of the landward limb is the result of extensive internal deformation.

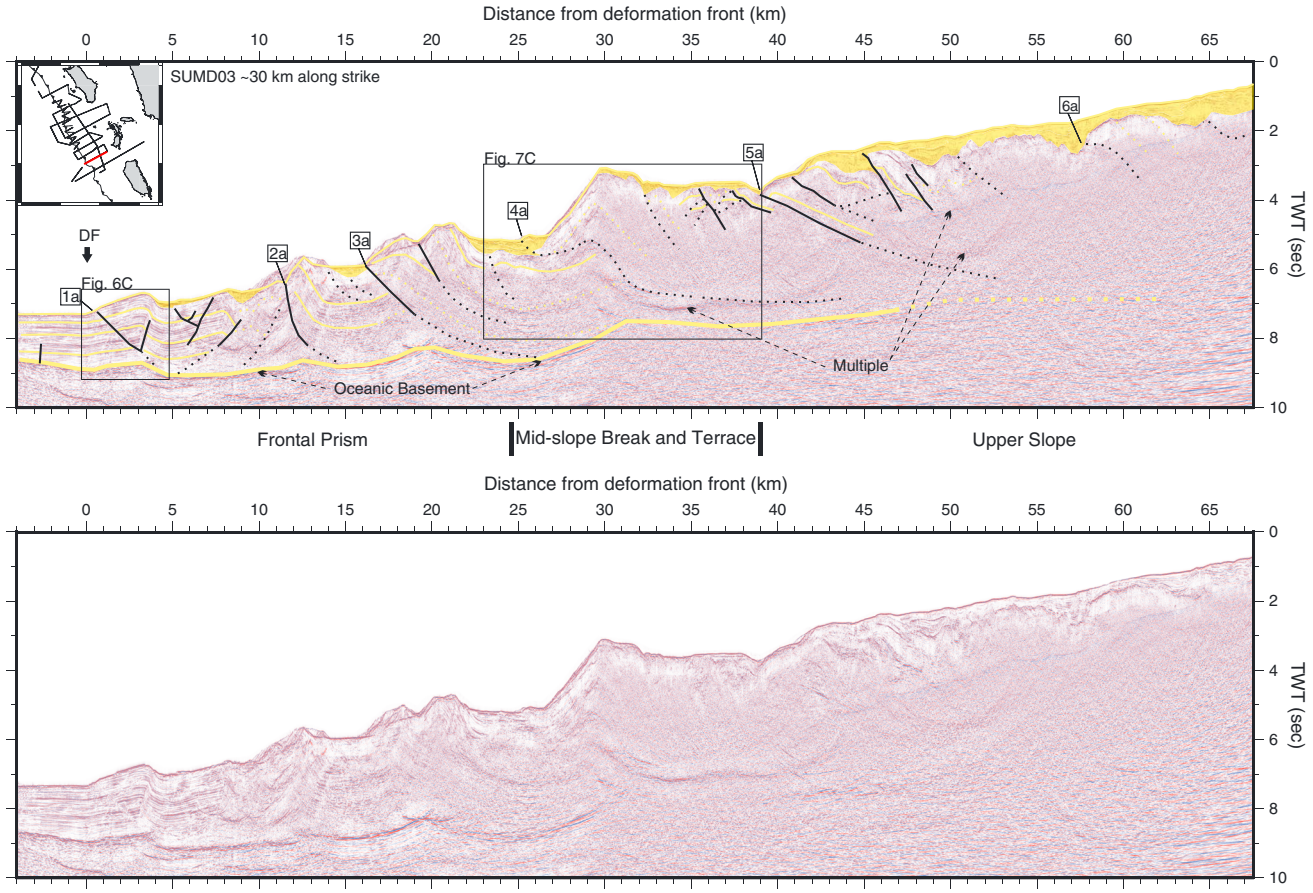

Figure 2. Seismic line SUMD03 showing the imbricate thrust structure of the frontal prism and belt-bounding major faults. (a) Interpreted and (b) uninterpreted, data are 1:1 at 4 km/s. The yellow lines represent sedimentary layering/lithologic boundaries, the yellow shaded polygons are packages of slope sediment, and the black lines are faults. The horizontal distance is measured from the deformation front which is marked DF.

Fault 5a is located ~40 km from the DF and marks a change to a more uniform seafloor slope. It has a negative polarity and variable strength fault plane reflection, and the hanging wall contains several shorter-wavelength (2–5 km) faults and folds. The seafloor landward of Fault 5a is smoother due to increased draping by forearc high-derived sediment and presumed reduced activity of prism thrusts. The prism seismic character is dominantly chaotic and is obscured by residual multiple noise. A relatively undeformed slope sediment package (up to 400 m thick) drapes the wedge from Fault 5a to the end of the line.

3.3. SUMD14

Line SUMD14 is located near the middle of our study area (~115 km along strike); we show a section of the line extending from 3.5 km seaward of the DF to 74.5 km landward into the outer forearc wedge (Figure 3). The incoming sedimentary section is 1.8 km thick at the trench, and the top of the oceanic basement is imaged much farther landward (~70 km) below the prism than on the other lines. The prism structure is dominated by cross-cutting landward and seaward dipping faults producing a complex deformation pattern. The thrust faults, coincident with the primary bathymetric ridges, have a spacing of 4–12 km and are labeled in Figure 3.

The outermost 10 km of the wedge is cut by two seaward dipping faults (1f and 1.5f), which sole into the top of oceanic basement and have a spacing of ~4 km. A possible negative polarity fault plane reflection is observed along Fault 1f, whereas Fault 1.5f is apparently nonreflective. The hanging wall anticlines associated with Faults 1f and 1.5f are well imaged and consistent with landward vergent deformation.

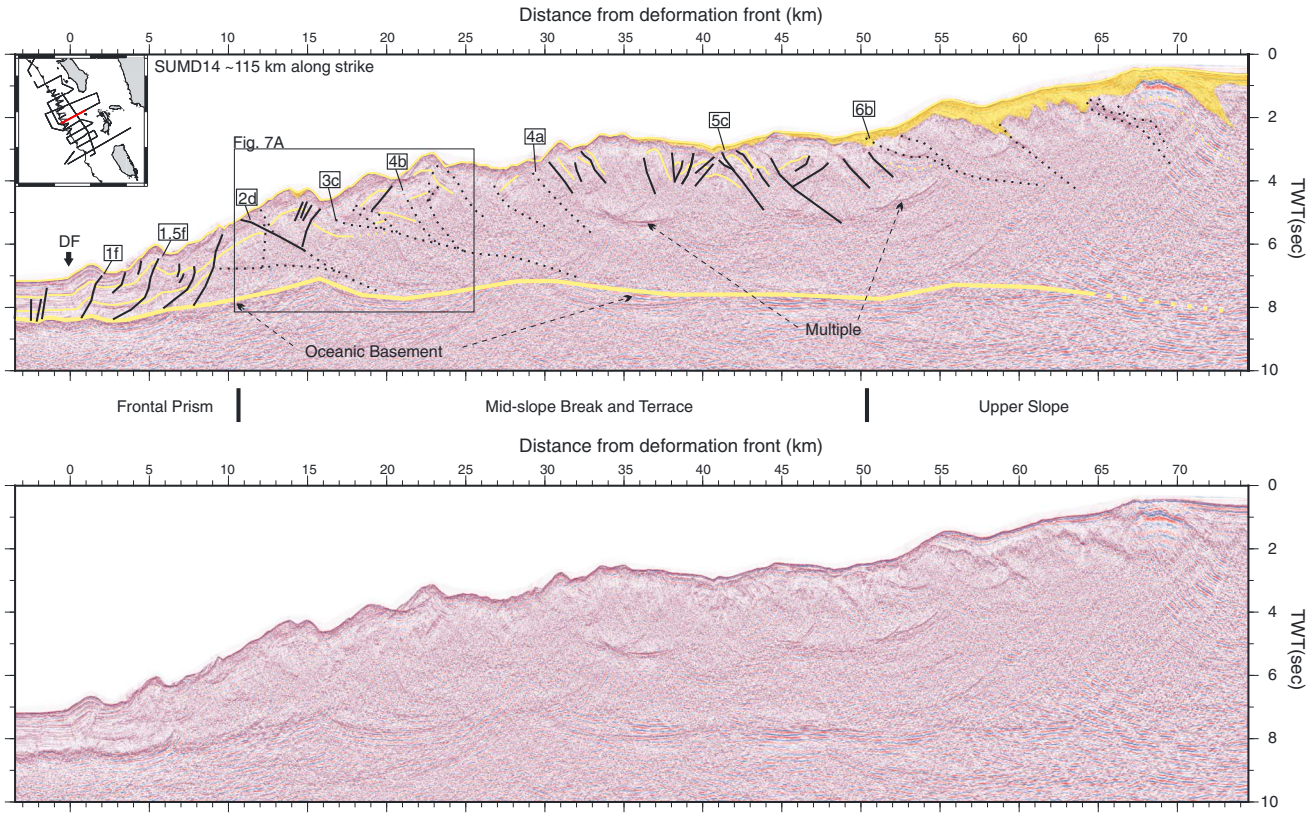

Figure 3. Seismic line SUMD14 showing the dominantly landward vergent imbricate thrust structure of the frontal prism, which is crosscut by the out-of-sequence midslope break fault. The wide midslope terrace is underlain by an apparently increased reflectivity oceanic basement. (a) Interpreted and (b) uninterpreted, data are 1:1 at 4 km/s. Symbology used is the same as in Figure 2.

From 10 to 25 km landward of the DF, the prism faulting pattern is complex and both landward and seaward dipping faults are observed. Faults 2d, 3c, and 4b are coincident with significant bathymetric ridges and a thickening of the prism, and are interpreted as major faults. The major faults are shown as landward dipping based on the orientation of deeper reflector packages interpreted as blocks of coherent sediment. Seaward dipping faults in the hanging wall(s) of the major Faults 2d and 3c appear to be crosscut by the major landward dipping faults (i.e., Fault 2d cuts a seaward dipping fault in the footwall at ~12 km, and Fault 3c cuts a seaward dipping fault in the hanging wall at ~19 km).

Between 25 and 50 km from the DF, the seafloor is fairly flat with three ~7 km wide terraces overlain by thin slope sediments (up to 200 m thick) and separated by gentle, fault-related ridges. Fault 4a can be traced on the bathymetry from SUMD03 and outcrops on the seafloor at 39 km from the DF; along SUMD14, the fault is much less prominent, and there is no obvious fault plane reflection. From 53 km landward, the seafloor slope increases and becomes more uniform, and the slope sediment package (vertical) thickness increases to ~0.3–1 km.

3.4. SUMD19

Line SUMD19 is the northernmost line in our study area (~245 km along strike) and extends from 5 km seaward of the DF to 55 km landward into the outer forearc wedge (Figure 4). The incoming sedimentary section is 2.8 km thick at the trench, and the top of the oceanic basement is imaged for ~35 km below the prism. The complex fault structures are composed of several landward dipping faults and associated folds with a spacing of 8–16 km (Figure 4).

The outermost 20 km of the wedge is cut by two named fault structures with a spacing of ~8 km. These two fault structures (2g and 3d) are both composed of several landward dipping faults which sole into the oceanic basement. The frontal thrust (2g) appears to have a negative polarity fault plane, whereas the other, more

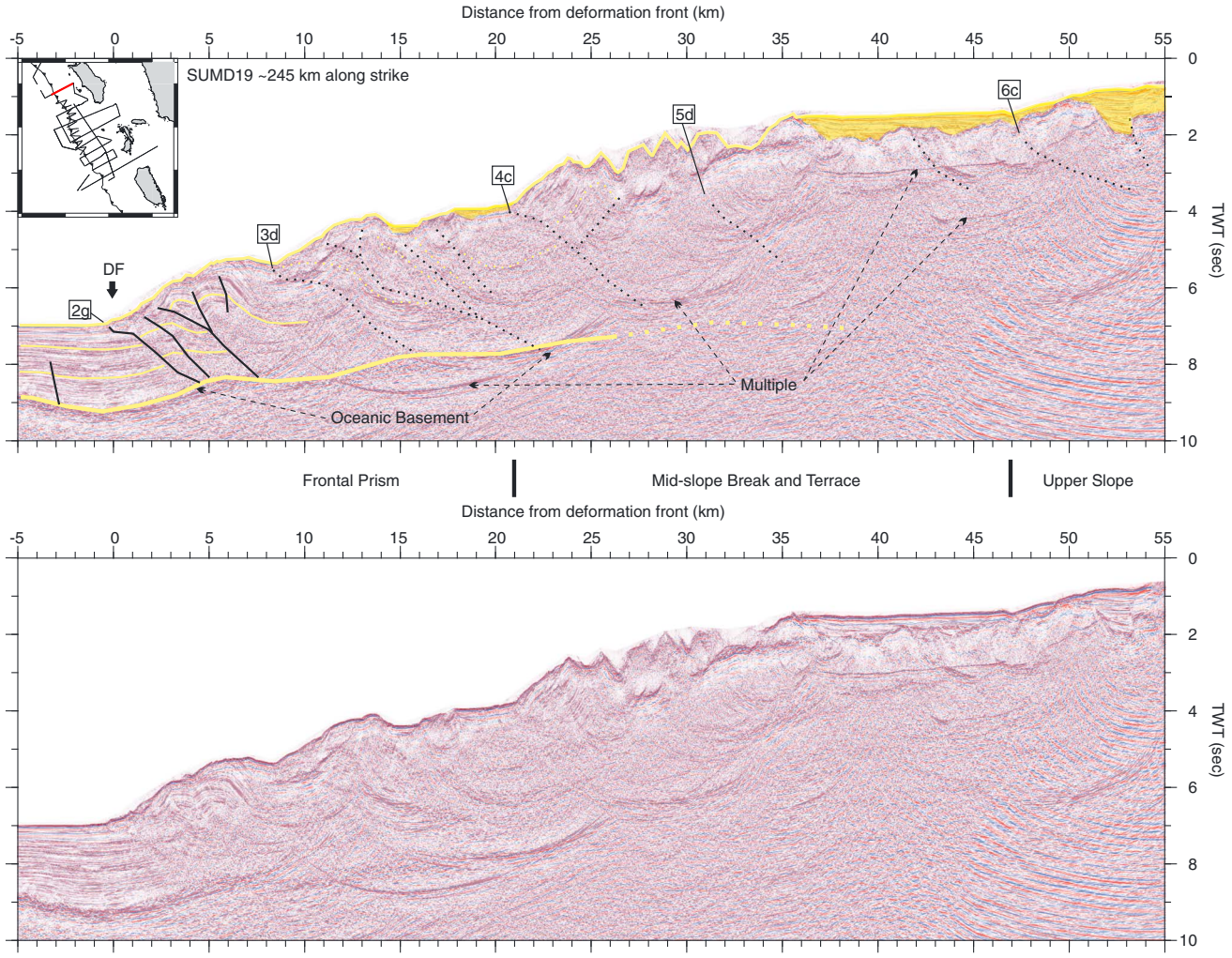

Figure 4. Seismic line SUMD19 showing the complex structure of the frontal prism and the poor imaging of the midslope break and upper slope-bounding faults. (a) Interpreted and (b) uninterpreted, data are 1:1 at 4 km/s. Symbology used is the same as in Figure 2.

landward, fault planes are nonreflective or poorly imaged. The seafloor surface in the outer 20 km of the prism is gently folded and has little to no slope sediment cover. From 20 to 36 km landward of the DF, increased erosion results in a much more rugose seafloor, and the underlying prism structure is obscured by major out-of-plane and multiple reflections making the interpretation uncertain in this area. An undisturbed slope basin extends from 36 to 46 km, and at the landward edge of the basin, the seafloor begins to gently slope upward. The prism underlying the landward portion of the line is dominated by chaotic seismic reflections with intermittent landward dipping reflections overlain by up to ~1 km of slope sediment.

3.5. Across and Along Strike Variability of Prism Structure

The accretionary prism offshore central Sumatra is characterized by complex deformation structures, which vary rapidly along and across strike (Figure 5a). We identify and use two relatively continuous morphological features coincident with major faults, the midslope break and upper slope-bounding fault, to subdivide the prism into three strike-parallel belts: the frontal prism, midslope break and terrace, and upper slope (Figure 5b). The frontal prism typically comprises a series of imbricate thrusts, which appear to sole into the sediment-oceanic basement interface and vary considerably along and across strike (Figure 6). The landward termination of the frontal prism is marked by a relatively high offset fault or fault network, which produces a clear midslope break (Figure 7). We define the upper slope as the portion of the wedge between the midslope terrace and crest of the outer forearc high (forearc island chain). The seaward boundary is marked

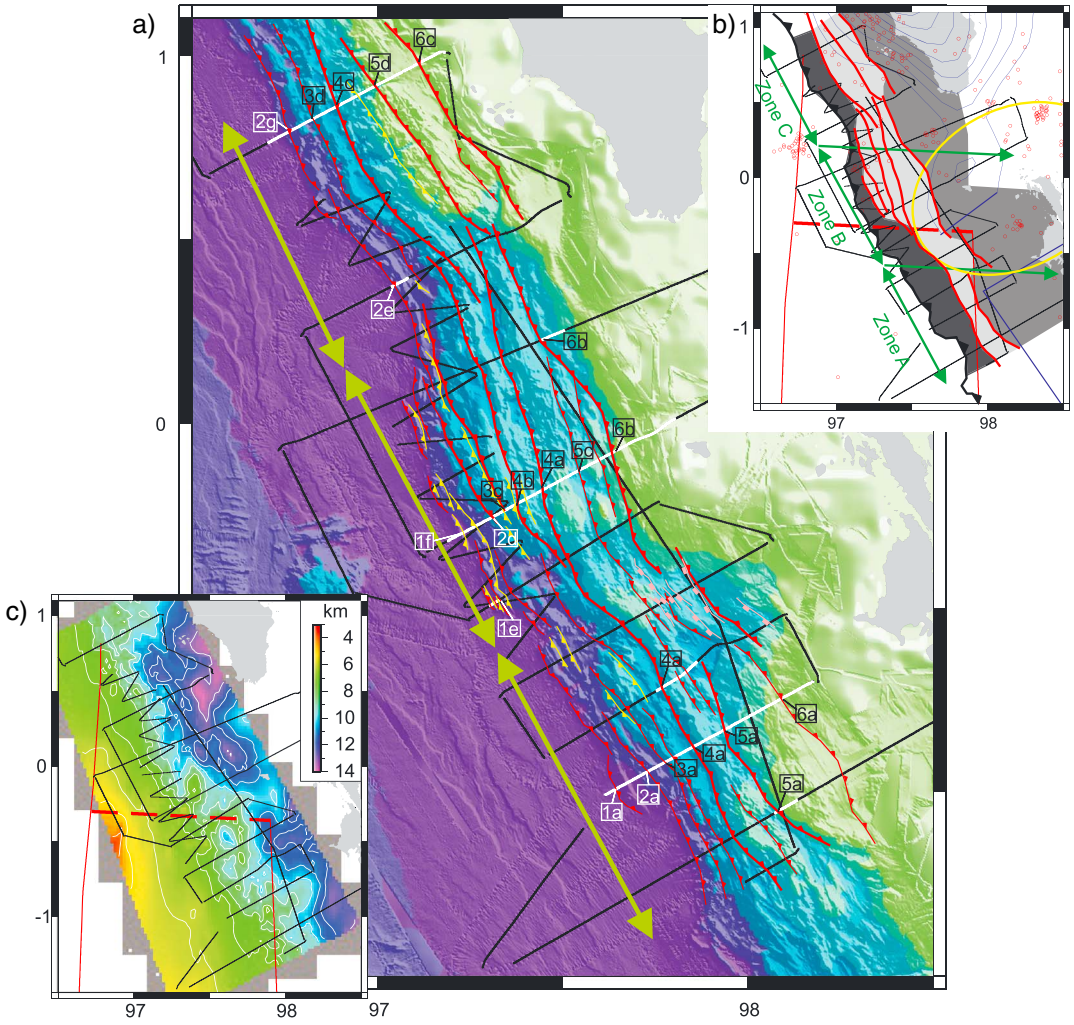

Figure 5. (a) Interpreted faults shown on bathymetry, (red: landward dipping, yellow: seaward dipping, and pink: normal), fault labels correspond to seismic lines shown in Figures 2–4 and 6–8, major faults are indicated by a thicker fault trace, and the green arrows indicate the extent of Zones A–C. (b) Extent of defined belts and zones (frontal prism: dark shading, midslope break and terrace: light shading, and upper slope: medium shading) with the incoming Wharton Fossil Ridge (dashed red lines) and associated fracture zones (solid red lines), and seismicity information including (blue) slip contours of the 2005 earthquake [*Hsu et al.*, 2006], approximate slip area (blue rectangle) of the 1797 earthquake [*Natawidjaja et al.*, 2006], area of the Batu Segment Boundary Zone (yellow ellipse), and local network aftershocks from *Lange et al.* [2010] (red circles) and *Tilmann et al.* [2010] (red squares). (c) Depth to top of oceanic basement calculated with three-layer velocity model (see text for details) and the incoming Wharton Fossil Ridge and associated fracture zones.

by the upper slope-bounding fault, a variably reflective fault reaching the seafloor at the base of this upper slope (Figure 8). The upper slope-bounding fault typically lacks a hanging wall scarp but coincides with a thickening of the wedge. The prism underlying the upper slope is typically composed of weak landward dipping or chaotic accreted sediment layer reflections that are truncated at the base of the slope sediment section or at the seafloor. The upper slope seafloor shows little variation in morphology and is relatively smooth.

Along strike variation in the dominant vergence sense of the frontal prism thrust folds and the seafloor morphology are used to further subdivide the prism into three along-strike zones: Zone A, Zone B, and Zone C (Figure 5b). The variation within and between each belt and zone is described below in more detail.

3.5.1. Frontal Prism Structure

The frontal prism contains a series of imbricate thrust structures in a 10–25 km wide belt. The trend of the deformation front is locally variable, and a trench salient (~80–160 km along strike) and reentrant

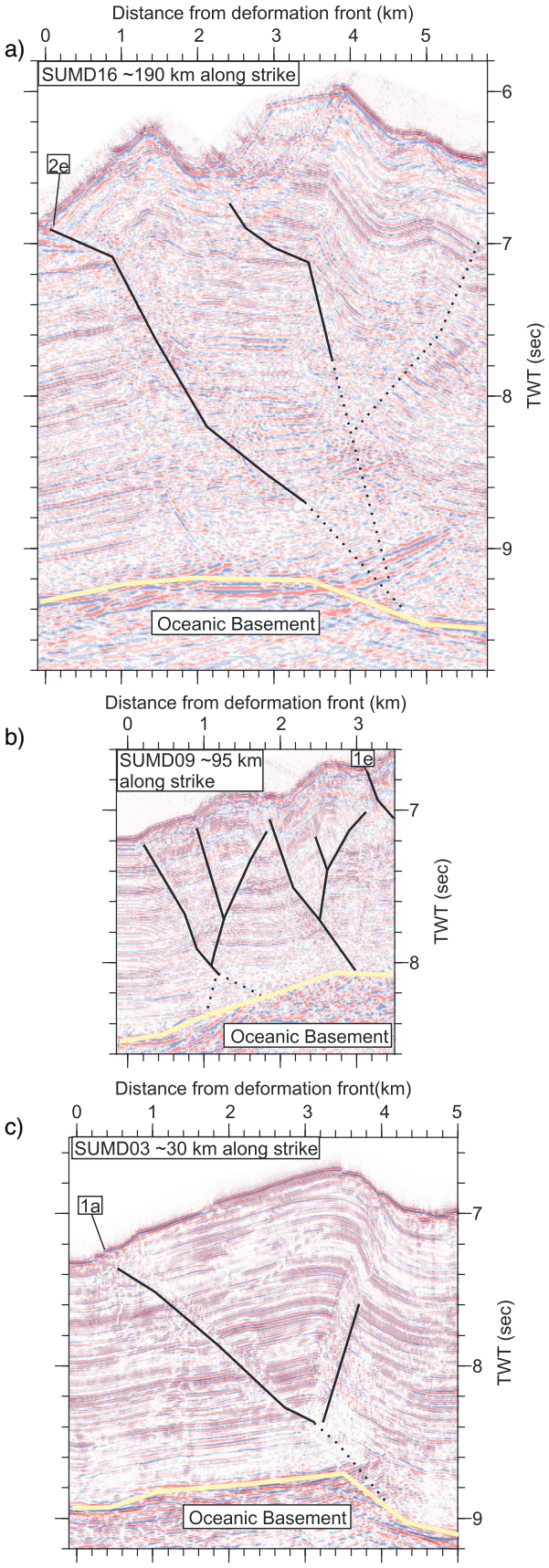

(~160–190 km) are observed on the bathymetric data (Figure 1). The frontal thrusts typically extend less than 25 km along strike; have seaward, landward, or variable dip/fold vergence direction; and, where clearly defined by offset stratigraphy, have negative polarity or nonreflective fault plane reflections. Landward of the frontal thrust, increasing fault displacement results in the linking of faults with similar orientations and increasing the along strike continuity of bathymetric ridges (Figure 5a). Seismic image quality decreases with distance landward of the deformation front, and fault plane reflections landward of the frontal thrust are not always resolved.

In Zone A, the deformation within the frontal prism is distributed over a series of landward dipping thrusts with minor active deformation on seaward dipping faults and landward vergent folds. Seaward dipping faults and landward vergent folds typically occur together, but we also observe some examples of seaward dipping faults with poorly developed (landward vergent) hanging wall anticlines (e.g., Figure 3; ~7 km), and landward vergent folds with little to no observable displacement on seaward dipping faults (Figure 6c).

Zone B is coincident with the trench salient (~80–160 km), and an increase in the occurrence of seaward dipping faults and landward vergent folds results in dominantly landward vergent (Figure 3) and/or symmetric structures (Figure 6b). In the northern half of Zone B, the seaward dipping faults are present with poorly developed landward vergent hanging wall anticlines.

In Zone C, the frontal prism faults are dominantly landward dipping and produce prominent hanging wall structures (Figure 5a and Figure 6a). The frontal structures are more complex than those to the south and are composed of

Figure 6. Seismic examples showing the variability of frontal structures. (a) SUMD16, (b) SUMD09, and (c) SUMD03, data are 1:1 at 4 km/s. Symbology used is the same as in Figure 2.

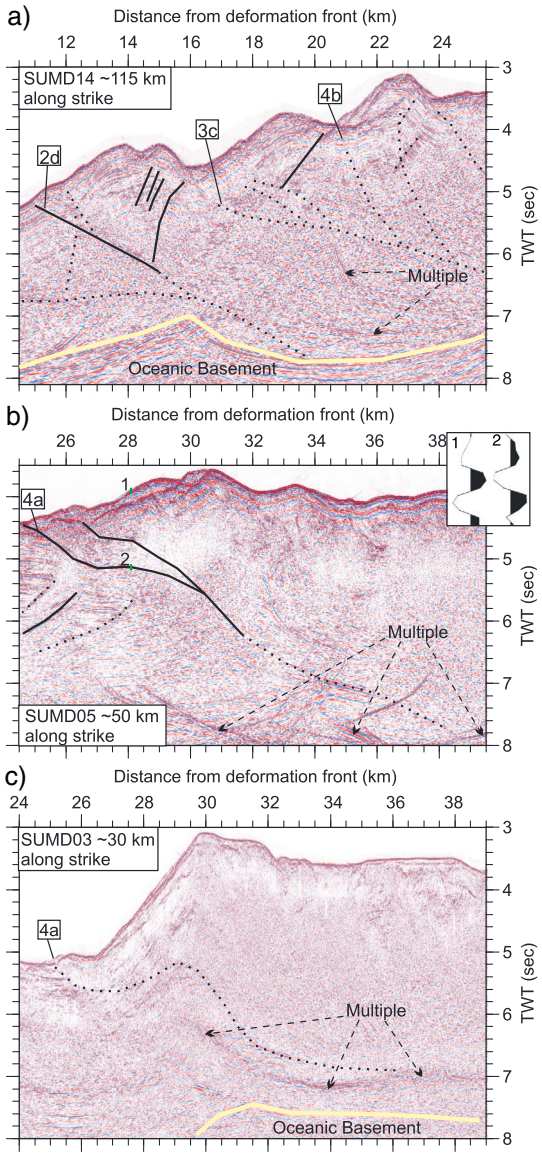

Figure 7. Seismic examples of the midslope break faults. (a) SUMD14, (b) SUMD05, and (c) SUMD03, data are 1:1 at 4 km/s. Inset shows the comparison of seabed and fault waveforms from the indicated locations, trace length is 100 m/s, and amplitudes are scaled to be comparable. Symbology used is the same as in Figure 2.

multiple faults and complexly folded structures (Figure 4 and Figure 6a). The southern half of Zone C is coincident with the trench reentrant (~160–190 km) and the thickest incoming sedimentary section within our study area (~3.1 km; Figure 6a).

3.5.2. Midslope Break and Terrace Structure

In Zone A, the midslope break is a prominent morphological feature and results from displacement along a single fault (Fault 4a) that can be traced along strike for ~70 km. Shallow hanging wall reflectors underlying the terraced area are intensely faulted and folded, whereas the deeper hanging wall has a chaotic seismic reflection character (Figure 7c). The midslope break fault is coincident with a negative polarity reflector, which is imaged on SUMD05 and SUMD03 (Figures 7b and 7c, respectively).

In Zone B, the trace of the southern midslope break, Fault 4a, decreases in prominence and bends landward. The seafloor traces of Faults 2d, 3c, and 4b resemble a horsetail pattern, suggesting that they are splaying from Fault 4a just south of SUMD14 and resulting in a seaward shift of the morphologic midslope break (Figures 5a and 5b). The midslope break faults in Zone B do not have obvious fault plane reflections, and the hanging wall anticlines produce relatively smooth (i.e., minimal erosion) bathymetric ridges.

In Zone C, the MCS data do not image the faulting, producing the midslope break well; the bathymetry suggests that the structure is complex and involves several faults. The presence of the midslope break faults (4c and 5d) is inferred from the thickened prism under the terrace (Figure 4) and the seafloor ridge geometry (Figure 5). The Zone C midslope break is presumed to be the result of displacement on several faults and is a prominent feature resulting in a shallower terrace level than observed to the south. Seafloor traces of Faults 4a, 4b, 4c, 5c, 5d, 6b, and 6c indicate a major change in fault-related strain distribution near the Zone B and Zone C boundaries. Faults 4b, 4a, and 5c are overthrust by Faults 4c, 5d, and 6b, respectively (Figure 5a).

Throughout our study area, the midslope terrace is overlain by flat-lying or very gently folded slope sediments, indicating that the wedge is not presently undergoing a significant internal deformation below the terrace. One exception is in Zone B, where midslope break-associated faulting extends over a broader zone into the terrace. In Zone B, we also note potentially increased reflectivity of the plate boundary reflection, which is well imaged beneath the midslope terrace and into the upper slope belt, to ~65–70 km (~15 km depth; Figure 3). Within Zone A, minor normal faulting below the midslope terrace has resulted in the formation of a shallow graben (Figure 5a, pink faults).

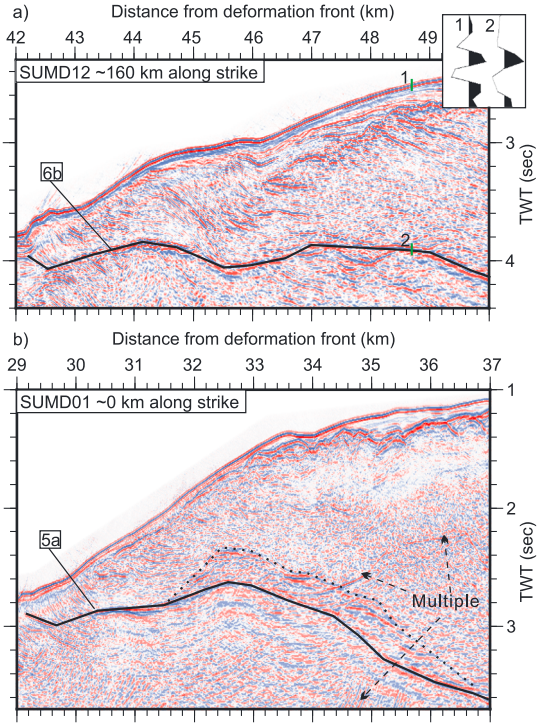

Figure 8. Seismic examples of the upper slope-bounding fault. (a) SUMD12 and (b) SUMD01, data are 1:1 at 4 km/s. Inset shows the comparison of seabed and fault waveforms from the indicated locations, trace length is 100 m/s, and amplitudes are scaled to be comparable. Symbology used is the same as in Figure 2.

3.5.3. Upper Slope-Bounding Fault and Upper Slope Structure

The upper slope-bounding fault coincides with a thickening of the wedge section and the transition to a relatively uniform/smooth upper slope. The upper slope-bounding faults lack a prominent hanging wall scarp, and the sedimentary reflectors in the hanging wall are truncated at the base of the slope sediment section (Figures 8a and 8b), indicating a decreased fault slip rate and/or increased erosion of the hanging wall. In the north of our study area, the upper slope-bounding fault steps landward (to Fault 6c), placing it on the edge of our seismic coverage, where the fault plane is obscured by the seabed multiple.

The individual segments of the upper slope-bounding fault exhibit variable seismic character. In Zone A, a weak to negative polarity fault plane reflection is observed on SUMD03 (Figure 2), and on SUMD01, a fault zone composed of a package of reflections is imaged (Figure 8b). On SUMD12 in Zone B, a relatively strong positive polarity fault plane reflection is imaged ~17 km landward of its seafloor expression beneath the upper slope (~6 km depth; Figure 8a).

4. Discussion

4.1. Along Strike Variability of Frontal Prism Structures

The only active seaward dipping faults and landward vergent folds are within the frontal prism belt of our study area. Seaward dipping faults and landward vergent folds imaged within the midslope break and terrace and upper slope belts are inactive, minor structures or present as backthrusts in the hanging walls of major structures. The nature of frontal prism structures (i.e., vergence sense, fault dip direction, and fault zone complexity) often changes from line to line (~20–30 km spacing) within the frontal prism belt. Fault dip direction does not seem to vary systematically along strike, although we do recognize increased deformation associated with seaward dipping faults and landward vergent folds in the Zone B frontal prism.

Seaward dipping faults and landward vergent folds are occasionally observed in the frontal prism of Zone A (Figure 5a). On SUMD03, the frontal structure is a landward vergent fold crosscut by a negative polarity landward dipping reflector (Figure 6c), suggesting that the deformation has recently transferred to a newly initiated landward dipping fault (i.e., the negative polarity reflector). The minor occurrences of landward vergent structures in Zone A suggest that the temporal extent of landward vergent deformation is shorter (i.e., landward vergent structures are younger or currently inactive); landward vergent structures have lower strain rates (relative to seaward vergent structures), or both.

In Zone B, seaward dipping faults/landward vergent folds are well developed in the frontal prism (Figure 5a and Figure 6b). The imbricate sequence of seaward dipping thrusts/landward vergent folds, which comprise the frontal prism, is crosscut by a landward dipping fault(s) at the midslope break. The increased occurrence of seaward dipping thrusts and landward vergent folds in the frontal prism suggests that landward vergent deformation is dominant in early prism development in Zone B and persists until material reaches the midslope break.

In Zone C, the frontal structures are complex and include both the seaward and landward dipping faults, and the dominant faults are typically landward dipping (Figure 6a). The bathymetric relief of the Zone C frontal structures is greater than those in Zones A and B to the south indicating higher net displacement, either due to a longer period of activity and/or higher slip rates.

Seaward dipping faults and landward vergent folds are also observed in accretionary prisms offshore Washington-northern Oregon-northern California (Cascadia), northern Sumatra-Nicobar-Andaman, southern Chile, and northern Panama [*Gulick et al.*, 1998; *Henstock et al.*, 2006; *MacKay et al.*, 1992; *McNeill and Henstock*, 2014; *Moeremans et al.*, 2014; *Polonia and Torelli*, 2007; *Reed et al.*, 1990; *Seely*, 1977]. Offshore northern Sumatra, the Andaman Islands, southern Chile, and northern Panama landward and mixed vergence structures in the prism toe are often associated with wide sections of the prism and relatively low overall slope values [*Gulick et al.*, 1998; *McNeill and Henstock*, 2014; *Polonia and Torelli*, 2007; *Reed et al.*, 1990]. On the Cascadia margin, landward and mixed vergence in the prism toe is generally concentrated in areas with high-sediment input from the Astoria, Nitinat, and Eel River fans [*Gulick et al.*, 1998; *MacKay et al.*, 1992; *Seely*, 1977].

Models for the development of landward vergence in the frontal prism require a weak basal detachment, and at Cascadia margin, it is suggested that an apparently overpressured horizon near the base of a thick incoming sedimentary section acts as the plate boundary décollement [*Gutscher et al.*, 2001; *MacKay*, 1995; *Seely*, 1977]. Similarly, offshore northern Sumatra landward vergence is associated with a thick incoming section and a potentially overpressured sediment layer [*Dean et al.*, 2010; *Henstock et al.*, 2006; *McNeill and Henstock*, 2014]. In contrast to much of the Cascadia and north Sumatran margins, landward vergence in our study area is most common in Zone B, where the sedimentary section is thinnest, and the majority of trench sediments are diverted off the basement high associated with the WFR to the adjacent trench depocenters. Therefore, it is unlikely that an overpressured horizon is present within the sediment section; if the development of landward vergence in our study area is associated with a weak basal detachment, we need a different model to explain its occurrence.

Along SUMD14 (Zone B), a relatively well imaged plate boundary reflection can be traced up to 70 km landward of the DF, below the accretionary prism (Figure 3). On the other lines in our study area, the plate boundary can typically be traced ~35–50 km landward of the DF. This difference in plate boundary imaging/reflectivity suggests that there may be a change in the physical properties or along-strike variations in wave transmission/attenuation and/or signal-to-noise ratio. If there is a change in the physical properties of the plate boundary, it may be similar to the increased plate boundary reflectivity observed along the Hikurangi margin associated with excess fluids [*Bell et al.*, 2010] and the general increases in reflectivity associated with fluid-rich zones observed at Nankai and Barbados [*Bangs et al.*, 1999; *Moore and Shipley*, 1993].

In our study area, we observe scattered negative polarity fault plane reflections and discordant (crosscutting sedimentary reflections) negative polarity reflections throughout the prism (Figure 6c and Figures 7a–7c). The discordant reflectors resemble low offset faults observed in other areas but with no seismically resolvable offset, and we interpret these as low offset faults/fractures. Structural inversion can be ruled out as a cause of the negative polarity discordant reflections, and the negative polarity character may be indicative of enhanced porosity supported by fluid flow. A likely fluid source is diagenetic dehydration reactions that are probably occurring at the base of the incoming sediment section offshore north Sumatra [*Geersen et al.*, 2013], resulting in a high-amplitude negative polarity reflector within the incoming section [*Dean et al.*, 2010]. In Zone B (and to some extent in Zone A), the topographic relief of the oceanic basement (Figure 5c) results in a thinner sediment section, likely delaying the onset of the diagenetic dehydration reactions until after the material is subducted/accreted. If the plate boundary fault acts as a permeability barrier, focusing of fluid flow by the topographic relief of the WFR could potentially result in the observed increased plate boundary reflectivity and the localized area of increased landward vergence in the frontal prism in Zone B.

Along-strike changes in frontal prism vergence and plate boundary reflectivity suggest spatial changes in the physical properties of the frontal prism and/or the underlying plate boundary on the ~10–100 km scale. Although there is some uncertainty about the exact mechanisms, the data suggest that oceanic basement topography, incoming sediment thickness, and the location of onset of diagenetic dehydration reactions are all key factors controlling the nature of deformation within the frontal prism.

4.2. Out-of-Sequence Thrusting and Activity of Major Thrust Faults

In our interpretation of the prism structure, we identified two major thrust faults, the midslope break fault and the upper slope-bounding fault, which separate the prism into three belts. These faults tend to have a larger net displacement than the adjacent faults and are associated with prominent seafloor ridges and/or significant thickening of the wedge. The lack of sediment age data, and variable sedimentation and erosion rates limits our ability to precisely determine fault slip rates; we attempt to constrain relative fault activity and potentially slip rates by identifying the hanging wall fault scarps and/or the deformation of the shallowest slope sediment cover. By utilizing these techniques, we interpret a progressive decrease in ongoing deformation within the intervening belts from the deformation front to the outer forearc high. In this section, we examine the characteristics of the major midslope break and upper slope-bounding faults and propose a model for their evolution.

The midslope break is typically characterized by high net slip on one or more faults, which produces a prominent morphological slope break within the prism and suggests significant ongoing (present-day) slip. Conversely, the upper slope-bounding fault is not associated with a significant slope break or seafloor scarp; instead, we typically observe a decrease in seafloor roughness and an increase in the seafloor slope leading to a significant increase in wedge thickness across the upper slope. The significant increase in wedge thickness indicates that the upper slope-bounding faults are major structures that have accommodated relatively high net slip. Within the hanging wall of the upper slope-bounding faults, we commonly observe truncated sedimentary reflectors underlying thin slope sediments ($<$100 m thickness; Figures 8a and 8b), indicating that a significant erosion may be responsible for the lack of the prominent hanging wall scarp. The decreased prominence of the hanging wall scarp of the upper slope-bounding fault(s) suggests a lower rate of present-day slip, increased erosion, or both.

The structure of the midslope break and the displacement distribution across controlling faults vary from relatively large displacement along a single major fault producing a prominent slope break in Zone A to lower total displacement on multiple faults in Zone B. The lower total displacement along the midslope break faults in Zone B suggests that the midslope break faults in Zone B are less mature than in Zone A (or Zone C). In Zone B, the most seaward midslope break fault (2d) appears to crosscut the seaward dipping faults of the inner frontal prism (Figure 7a), suggesting that the midslope break faults in this zone are out-of-sequence thrusts (OOST). Within Zones A and C, the midslope break is more prominent due to higher net displacement along individual fault(s), and there is no clear cross-cutting relationship with the frontal prism faults and the midslope break faults may be in or out of sequence.

The geometry of the Zone A midslope break fault (4a) resembles that of the megasplay fault or OOST observed on the Kumano transect of the Nankai margin [*Bangs et al.*, 2009; *Gulick et al.*, 2010; *Park et al.*, 2002]. Both faults have seafloor outcrops located ~20–25 km from the deformation front; are steeply dipping near the seafloor, shallow in dip with depth; and are associated with a strong negative polarity fault plane reflection [*Park et al.*, 2002]. In Nankai, the negative polarity reflection along the megasplay fault plane is attributed to an underthrust underconsolidated and overpressured layer between the fault and the underlying oceanic basement and/or active fluid flow sourced from diagenetic dehydration reactions taking place at deeper levels [*Bangs et al.*, 2009; *Saffer and Tobin*, 2011]. Along SUMD03, we roughly estimate a depth of ~6 km for the change in fault plane reflectivity using a simple three-layer velocity model (see section 2). Diagenetic dehydration reactions associated with the updip limit of seismogenesis are often taken to start at roughly ~5 km depth, although this can be modified by the local thermal regime [*Moore et al.*, 2007]. The fluid released at a depth of ~5 km may become trapped along the fault plane, or it may migrate updip along the fault contributing to the negative polarity of the shallower fault plane reflection. We interpret the negative polarity midslope break fault plane observed in Zone A to be a result of a combination of structural inversion across a thrust fault and excess fluids derived from dehydration reactions occurring at ~5 km depth.

The fault plane of the upper slope-bounding fault has variable character, including the sections of positive polarity fault plane reflections (Figure 8a) and thicker reflective sections that have distinct seismic character from the footwall and hanging wall blocks (Figure 8b). Positive polarity fault planes are unusual in accretionary prisms, where a significant thrust displacement in mature fault systems typically generates an impedance decrease across faults expressed as negative polarity fault planes. Outcrops of fossil OOST in

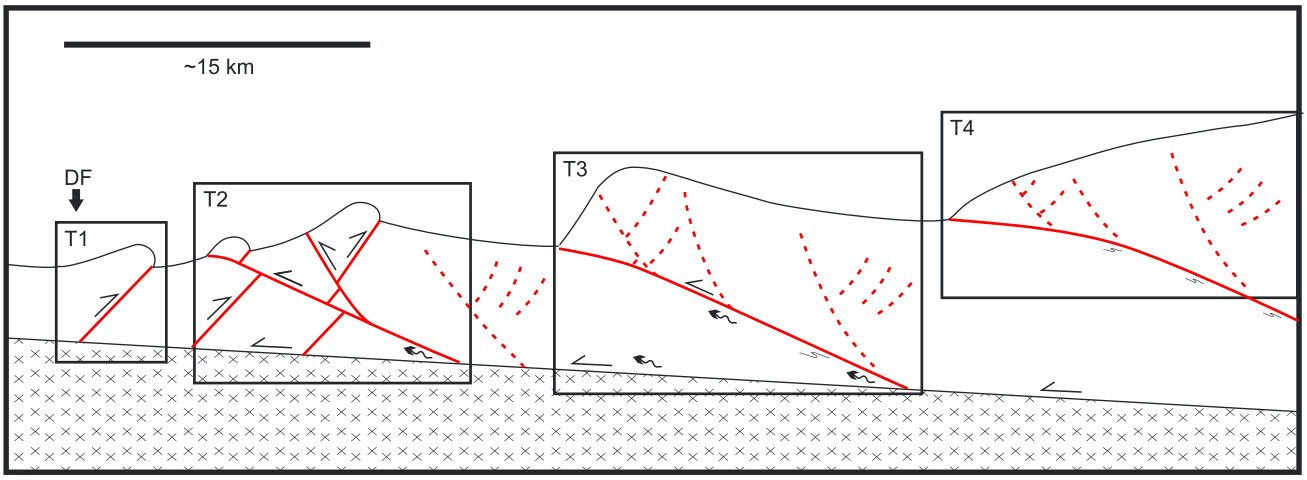

Figure 9. Schematic model of the spatiotemporal development of major faults within the north-central Sumatran accretionary prism. T1: fault initiation at the deformation front. T2: major fault initiated out of sequence crosscutting earlier structures. T3: increasing net slip and relatively high slip rate on major structure results in a significant structural thickening of the wedge and a prominent seafloor scarp. Underthrust sediments undergo diagenetic dehydration reactions introducing fluids to system, which either migrate updip or become trapped along the plate boundary or major prism faults. T4: decreasing slip rate on major fault and/or increasing erosion of hanging wall reduces prominence of hanging wall scarp.

Japan and Alaska juxtapose rocks with varying thermal histories indicating displacements >10 km; these faults are associated with footwall shear zones or melanges that vary in thickness from tens of meters to several kilometers and are characterized by intense shearing and quartz and carbonate cementation that decreases in intensity away from the fault zone [*Kondo et al.*, 2005; *Rowe et al.*, 2009]. Extensive cementation decreases porosity and increases crystallinity (rigidity/shear modulus) resulting in increased velocity, density, and therefore impedance. The presence of a similar type of asymmetric deformation around the mature upper slope-bounding fault could be a possible explanation for the observed positive polarity fault plane reflections. Similar processes are thought to be responsible for the decrease in amplitude with depth observed along the Nankai-Muroto décollement reflection [*Bangs et al.*, 2004].

We interpret the midslope break and upper slope-bounding faults as major fault zones accommodating a significant component of convergence within the prism. In Zone B, the immature midslope break fault crosscuts older frontal prism faults, indicating that in this area of the prism, the major faults are out of sequence. The Zone A midslope break fault (4a) is a high net slip structure with apparently high current slip rate and is characterized by a strong negative polarity fault plane reflection at shallow (<7–8 km) depths. The upper slope-bounding faults in Zones A and B (5a and 6b) are also a high net slip structure, but in contrast to the midslope break fault, it has apparently low to nil present-day slip rate and variable fault plane reflectivity including positive polarity sections. The phases of development of these major faults are captured at different stages of maturity on individual MCS seismic profiles, and we use their characteristics to model major prism fault development and the development of the accretionary prism as a whole.

In our proposed model of formation, we represent the different time stages of fault development (Figure 9). The development of the major fault structures is modeled assuming that the upper slope-bounding fault represents the most mature end-member and evolves from structures similar to the observed midslope break faults. Faulting initially occurs at the deformation front (Figure 9; T1), and although only seaward dipping faults are shown in this schematic model, landward dipping faults may also form at this stage. At T2 (Figure 9), the immature midslope break faults are formed out of sequence, crosscutting the older seaward dipping frontal prism faults (e.g., Faults 2d, 3c, and 4b; Figure 7A). The mature midslope break fault develops through slip localization either on one of these OOST or possibly along preexisting in sequence landward dipping faults. At T3 (Figure 9), temperatures and pressures increase, and material underthrust along the now more mature midslope break fault undergo diagenetic dehydration reactions. As fluids are liberated, they may flow upward along the fault plane or become trapped along the fault plane, decreasing the effective normal stress and effective fault friction (e.g., Fault 4a; Figures 7b and 7c). Continued fault displacement and progression into the interior of the wedge results in a significant uplift and erosion of the hanging wall (Figure 9; T4), producing the

observed upper slope-bounding fault structure and morphology (i.e., Faults 5a and 6b; Figures 8a and 8b). Eventually, fault displacement ceases on this major fault and is transferred to the underlying plate boundary décollement and/or a younger (seaward) major structure.

4.3. Relationship to Seismicity

To examine the relationship between the observed structure and morphology of the outer prism (observed across the Zones A, B, and C) to the seismicity observations, it is useful to project the Zone boundaries downdip. There are three potential methods for projection: (1) parallel to the Australian-Sundaland plate relative motion (no slip partitioning), (2) perpendicular to the trench and parallel to the Australian-Sumatran sliver plate relative motion (fully slip-partitioned model), or (3) along the WFR trend. In Figure 5, we use method 3 and project along the WFR, because our data suggest that it may be partially controlling variations in the plate boundary physical properties which relate to the zone boundaries (i.e., decreased effective normal stress/friction and frontal prism landward vergence).

Zone C of our study area is coincident with the Nias segment, where the updip limit of the seismogenic zone is apparently defined by a concentration of locally recorded earthquakes west of Nias Island that are roughly coincident with the plate boundary below the 500 m bathymetry contour [*Lange et al.*, 2010; *Tilmann et al.*, 2010]. This band of earthquakes is located below the upper slope as defined in this study (Figure 5b), suggesting that the upper slope may be coincident with the onset of seismogenesis. Models of coseismic slip for the 2005 earthquake indicate that coseismic slip extended farther seaward (i.e., into the midslope terrace) than the updip limit of seismogenesis as defined by aftershocks [e.g., *Hsu et al.*, 2006]. In this area, the increased energy release on the high slip patch beneath Nias could cause rupture to propagate farther into the potentially velocity strengthening shallow plate boundary.

In the Batu Segment Boundary Zone, there is limited information on seismicity from earthquake ruptures, but GPS deformation suggests that the area has lower coupling than the adjacent Nias and Mentawai segments [*Chlieh et al.*, 2008]. The downdip projection of Zone B along the WFR is roughly coincident with the area of decreased coupling below Batu (Figure 5b). It may be that the mechanisms responsible for weakening the plate boundary below the frontal prism (i.e., delayed diagenetic dehydration reactions and fluid flow focusing by oceanic basement topography) are also occurring at deeper levels.

In the Mentawai segment, there is limited information on the updip limits of coseismic slip and seismogenesis. Coral geodetic records primarily constrain the along-strike extent of the 1797 earthquake rupture [*Natawidjaja et al.*, 2006], and there is little current seismicity to define the updip limit of the seismogenic zone [*Lange et al.*, 2010]. If the relationship between the updip limit of seismogenesis and the upper slope-bounding fault observed in the Nias segment (Zone C) holds in the Mentawai segment (Zone A), we can estimate the updip limit of the seismogenic zone. In this case, the estimated updip limit of seismogenic zone in Zone A (i.e., the upper slope-bounding fault) would be located slightly closer to the trench (~30–40 km; Figure 2 and Figure 5b) than observed in Zone C (~40–45 km; Figure 4 and Figure 5b).

Tsunamigenesis in the Mentawai segment could potentially be related to the shallower updip limit of seismogenesis, the presence of major splay faults, and/or potentially varying plate boundary properties. The southern extension of Fault 4a is located near the areas inundated by the 1797 tsunami [*Newcomb and McCann*, 1987], and the slip along this fault could potentially have contributed to tsunami generation as suggested for the 1944 Tonankai tsunami [*Park et al.*, 2002]. Alternatively, the occurrence of landward and mixed vergence structures suggest that there may be a relatively weak shallow plate boundary (below the frontal prism and midslope break and terrace belts) in the Mentawai segment and the Batu Segment Boundary Zone, which may increase tsunami amplitude by allowing slip to easily propagate to shallower levels of the plate boundary [*Kanamori*, 2001].

5. Conclusions

Our examination of the north-central Sumatran margin (~1.5°S to 1°N) indicates that oceanic basement topography, incoming sediment thickness, and fluid content are key factors contributing to the development of the accretionary prism structures and, potentially, the nature of seismicity. Key observations and results are the following: (1) The accretionary prism is characterized by complex deformation structures which vary along and across strike on the scale of tens to hundreds of kilometers. (2) Changes in the dominant frontal

prism fault dip/fold vergence and seafloor morphology divide the prism into along-strike Zones, A, B, and C. (3) The midslope break and upper slope-bounding faults are significant, high net slip structures that accommodate a significant amount of convergence-related strain. They subdivide the prism into three strike-parallel belts: the frontal prism, midslope break and terrace, and upper slope. (4) The negative polarity fault plane reflections, observed along the sections of the midslope break fault, are attributed to fluids derived from the diagenetic dewatering of underthrust sediments. The presence of fluids may lower the effective fault friction. (5) The positive polarity fault plane reflections, observed along the sections of the upper slope-bounding fault, are attributed to the cementation of the more mature fault zone. (6) A model has been developed that describes the stages of major prism fault development. The major faults can be initiated in or out of sequence and are potentially important conduits for fluid flow within the prism, and the upper slope-bounding fault is more mature than the midslope break fault. (7) In the 2005 earthquake rupture segment, the upper slope-bounding fault coincides in map view with the updip limit of seismogenesis (as defined by aftershocks). (8) If the major midslope break fault slips coseismically, tsunami risk may be increased. (9) Landward vergent structures in the frontal prism of Zone B and increased reflectivity of the top of the downgoing plate suggest a fluid-weakened plate boundary associated with the subducting Wharton Fossil Ridge. (10) Tsunamigenesis in the Batu Segment Boundary Zone and Mentawai segment may be amplified by shallow slip of a weak plate boundary.

Acknowledgments

This work was funded by the Natural Sciences and Engineering Research Council of Canada, University of Southampton, and Natural Environment Research Council, grant NE/D004381/1. We thank the master and crew of the R/V *Sonne* for their assistance during cruises SO198 and SO200 and our partners BPPT, Jakarta, for their logistical assistance. We thank the Bundesanstalt für Geowissenschaften und Rohstoffe, supported by the Federal Ministry of Education and Research (BMBF), Germany grants 03G186A and 03G189A, for allowing the use of their bathymetric data in this study. The seismic reflection and bathymetric (UK) data presented in this study are lodged with the British Oceanographic Data Centre http://www.bodc.ac.uk. We thank the reviewers, Sean Gulick and Harold Tobin, and the Associate Editor, Gail Christeson, for providing useful constructive comments that have greatly improved the manuscript.

References

Bangs, N. L., T. H. Shipley, J. C. Moore, and G. F. Moore (1999), Fluid accumulation and channeling along the northern Barbados Ridge decollement thrust, *J. Geophys. Res.*, *104*(B9), 20,399–20,414, doi:10.1029/1999JB900133.

Bangs, N. L., T. H. Shipley, S. P. S. Gulick, G. F. Moore, S. Kuromoto, and Y. Nakamura (2004), Evolution of the Nankai Trough décollement from the trench into the seismogenic zone: Inferences from three-dimensional seismic reflection imaging, *Geology*, *32*(4), 273–276.

Bangs, N. L., G. F. Moore, S. P. S. Gulick, E. M. Pangborn, H. J. Tobin, S. Kuramoto, and A. Taira (2009), Broad, weak regions of the Nankai Megathrust and implications for shallow coseismic slip, *Earth Planet. Sci. Lett.*, *284*(1), 44–49.

Barnes, P. M., A. Nicol, and T. Harrison (2002), Late Cenozoic evolution and earthquake potential of an active listric thrust complex above the Hikurangi subduction zone, New Zealand, *Geol. Soc. Am. Bull.*, *114*(11), 1379–1405.

Bell, R., R. Sutherland, D. H. N. Barker, S. Henrys, S. Bannister, L. Wallace, and J. Beavan (2010), Seismic reflection character of the Hikurangi subduction interface, New Zealand, in the region of repeated Gisborne slow slip events, *Geophys. J. Int.*, *180*(1), 34–48.

Bilek, S. L., E. R. Engdahl, H. R. DeShon, and M. El Hariri (2011), The 25 October 2010 Sumatra tsunami earthquake: Slip in a slow patch, *Geophys. Res. Lett.*, *38*, L14306, doi:10.1029/2011GL047864.

Bock, Y., L. Prawirodirdjo, J. F. Genrich, C. W. Stevens, R. McCaffrey, C. Subarya, S. S. O. Puntodewo, and E. Calais (2003), Crustal motion in Indonesia from Global Positioning System measurements, *J. Geophys. Res.*, *108*(B8), 2367, doi:10.1029/2001JB000324.

Byrne, D. E., D. M. Davis, and L. R. Sykes (1988), Loci and maximum size of thrust earthquakes and the mechanics of the shallow region of subduction zones, *Tectonics*, *7*(4), 833–857, doi:10.1029/TC007i004p00833.

Chlieh, M., J. P. Avouac, K. Sieh, D. H. Natawidjaja, and J. Galetzka (2008), Heterogeneous coupling of the Sumatran megathrust constrained by geodetic and paleogeodetic measurements, *J. Geophys. Res.*, *113*, B05305, doi:10.1029/2007JB004981.

Cochran, J. R. (2010), Morphology and tectonics of the Andaman Forearc, northeastern Indian Ocean, *Geophys. J. Int.*, *182*(2), 631–651.

Collot, J.-Y., W. Agudelo, A. Ribodetti, and B. Marcaillou (2008), Origin of a crustal splay fault and its relation to the seismogenic zone and underplating at the erosional north Ecuador-south Colombia oceanic margin, *J. Geophys. Res.*, *113*, B12102, doi:10.1029/2008JB005691.

Davis, D., J. Suppe, and F. A. Dahlen (1983), Mechanics of Fold-and-Thrust Belts and Accretionary Wedges, *J. Geophys. Res.*, *88*(B2), 1153–1172, doi:10.1029/JB088iB02p01153.

Dean, S. M., L. C. McNeill, T. J. Henstock, J. M. Bull, S. P. S. Gulick, J. A. Austin, N. L. B. Bangs, Y. S. Djajadihardja, and H. Permana (2010), Contrasting decollement and prism properties over the Sumatra 2004-2005 Earthquake rupture boundary, *Science*, *329*(5988), 207–210.

DeMets, C., R. G. Gordon, and D. F. Argus (2010), Geologically current plate motions, *Geophys. J. Int.*, *181*(1), 1–80.

Faulkner, D. R., T. M. Mitchell, J. Behnsen, T. Hirose, and T. Shimamoto (2011), Stuck in the mud? Earthquake nucleation and propagation through accretionary forearcs, *Geophys. Res. Lett.*, *38*, L18303, doi:10.1029/2011GL048552.

Fitch, T. J. (1972), Plate convergence, transcurrent faults, and internal deformation adjacent to Southeast Asia and the western Pacific, *J. Geophys. Res.*, *77*(23), 4432–4460, doi:10.1029/JB077i023p04432.

Fuller, C. W., S. D. Willett, and M. T. Brandon (2006), Formation of forearc basins and their influence on subduction zone earthquakes, *Geology*, *34*(2), 65–68.

Geersen, J., L. McNeill, T. J. Henstock, and C. Gaedicke (2013), The 2004 Aceh-Andaman Earthquake: Early clay dehydration controls shallow seismic rupture, *Geochem. Geophys. Geosyst.*, *14*, 3315–3323, doi:10.1002/ggge.20193.

Gulick, S. P. S., A. M. Meltzer, and S. H. Clarke Jr. (1998), Seismic structure of the southern Cascadia subduction zone and accretionary prism north of the Mendocino triple junction, *J. Geophys. Res.*, *103*(B11), 27,207–27,222, doi:10.1029/98JB02526.

Gulick, S. P. S., N. L. B. Bangs, G. F. Moore, J. Ashi, K. M. Martin, D. S. Sawyer, H. J. Tobin, S. I. Kuramoto, and A. Taira (2010), Rapid forearc basin uplift and megasplay fault development from 3D seismic images of Nankai Margin off Kii Peninsula, Japan, *Earth Planet. Sci. Lett.*, *300*(1–2), 55–62.

Gulick, S. P. S., J. A. Austin, L. C. McNeill, N. L. B. Bangs, K. M. Martin, T. J. Henstock, J. M. Bull, S. Dean, Y. S. Djajadihardja, and H. Permana (2011), Updip rupture of the 2004 Sumatra earthquake extended by thick indurated sediments, *Nat. Geosci.*, *4*(7), 453–456.

Gutscher, M.-A., D. Klaeschen, E. Flueh, and J. Malavieille (2001), Non-Coulomb wedges, wrong-way thrusting, and natural hazards in Cascadia, *Geology*, *29*(5), 379–382.

Henstock, T. J., L. C. McNeill, and D. R. Tappin (2006), Seafloor morphology of the Sumatran subduction zone: Surface rupture during megathrust earthquakes?, *Geology*, *34*(6), 485–488.

Hsu, Y.-J., M. Simons, J.-P. Avouac, J. Galetzka, K. Sieh, M. Chlieh, D. Natawidjaja, L. Prawirodirdjo, and Y. Bock (2006), Frictional afterslip following the 2005 Nias-Simeulue Earthquake, Sumatra, *Science*, *312*(5782), 1921–1926.

Huiqi, L., K. R. McClay, and D. Powell (1992), Physical models of thrust wedges, in *Thrust Tectonics*, edited by K. R. Mcclay, pp. 71–81, Chapman and Hall, New York.

Ide, S., A. Baltay, and G. C. Beroza (2011), Shallow dynamic overshoot and energetic deep rupture in the 2011 Mw 9.0 Tohoku-Oki Earthquake, *Science*, *332*(6036), 1426–1429.

Kanamori, H. (2001), Energy budget of earthquakes and seismic efficiency, in *Earthquake Thermodynamics and Phase Transformations in the Earth's Interior*, edited by R. Teisseyre and E. Majewski, pp. 293–305, Academic Press, New York.

Kieckhefer, R. M., G. G. Shor, J. R. Curray, W. Sugiarta, and F. Hehuwat (1980), Seismic refraction studies of the Sunda Trench and Forearc Basin, *J. Geophys. Res.*, *85*(B2), 863–889, doi:10.1029/JB085iB02p00863.

Kondo, H., G. Kimura, H. Masago, K. Ohmori-Ikehara, Y. Kitamura, E. Ikesawa, A. Sakaguchi, A. Yamaguchi, and S. Y. Okamoto (2005), Deformation and fluid flow of a major out-of-sequence thrust located at seismogenic depth in an accretionary complex: Nobeoka Thrust in the Shimanto Belt, Kyushu, Japan, *Tectonics*, *24*, TC6008, doi:10.1029/2004TC001655.

Kopp, H., and N. Kukowski (2003), Backstop geometry and accretionary mechanics of the Sunda margin, *Tectonics*, *22*(6), 1072, doi:10.1029/2002TC001420.

Kopp, H., et al. (2008), Lower slope morphology of the Sumatra trench system, *Basin Res.*, *20*(4), 519–529.

Lange, D., F. Tilmann, A. Rietbrock, R. Collings, D. H. Natawidjaja, B. W. Suwargadi, P. Barton, T. Henstock, and T. Ryberg (2010), The Fine structure of the subducted investigator fracture zone in western Sumatra as seen by local seismicity, *Earth Planet. Sci. Lett.*, *298*(1–2), 47–56.

Lay, T., et al. (2005), The Great Sumatra-Andaman Earthquake of 26 December 2004, *Science*, *308*(5725), 1127–1133.

Liu, C.-S., J. R. Curray, and J. M. McDonald (1983), New constraints on the tectonic evolution of the eastern Indian Ocean, *Earth Planet. Sci. Lett.*, *65*(2), 331–342.

Loveless, J. P., and B. J. Meade (2011), Spatial correlation of interseismic coupling and coseismic rupture extent of the 2011 MW = 9.0 Tohoku-oki earthquake, *Geophys. Res. Lett.*, *38*, L17306, doi:10.1029/2011GL048561.

MacKay, M. E. (1995), Structural variation and landward vergence at the toe of the Oregon accretionary prism, *Tectonics*, *14*(6), 1309–1320, doi:10.1029/95TC02320.

MacKay, M. E., G. F. Moore, G. R. Cochrane, J. Casey Moore, and L. D. Kulm (1992), Landward vergence and oblique structural trends in the Oregon margin accretionary prism: Implications and effect on fluid flow, *Earth Planet. Sci. Lett.*, *109*(3–4), 477–491.

Marone, C., and D. Saffer (2007), Fault friction and the upper transition from seismic to aseismic faulting, in *The Seismogenic Zone of Subduction Thrust Faults*, edited by T. H. Dixon and J. C. Moore, pp. 346–369, Coumbia Univ. Press, New York.

McCaffrey, R. (2009), The tectonic framework of the Sumatran Subduction Zone, *Annu. Rev. Earth Planet. Sci.*, *37*(1), 345–366.

McCaffrey, R., P. C. Zwick, Y. Bock, L. Prawirodirdjo, J. F. Genrich, C. W. Stevens, S. S. O. Puntodewo, and C. Subarya (2000), Strain partitioning during oblique plate convergence in northern Sumatra: Geodetic and seismologic constraints and numerical modeling, *J. Geophys. Res.*, *105*(B12), 28,363–28,376, doi:10.1029/1999JB900362.

McNeill, L. C., and T. J. Henstock (2014), Forearc structure and morphology along the Sunda subduction zone, *Tectonics*, *33*, 112–134, doi:10.1002/2012TC003264.

Moeremans, R., S. C. Singh, M. Mukti, J. McArdle, and K. Johansen (2014), Seismic images of structural variations along the deformation front of the Andaman–Sumatra subduction zone: Implications for rupture propagation and tsunamigenesis, *Earth Planet. Sci. Lett.*, *386*, 75–85.

Moore, G. F., and J. R. Curray (1980), Structure of the Sunda Trench lower slope off sumatra from multichannel seismic reflection data, *Mar. Geophys. Res.*, *4*(3), 319–340.

Moore, G. F., and T. H. Shipley (1993), Character of the décollement in the Leg 131 area, Nankai Trough, in *Proc. ODP, Sci. Results*, edited by I. A. Hill et al., pp. 73–82, Ocean Drilling Program, College Station, Tex.

Moore, G. F., J. R. Curray, D. G. Moore, and D. E. Karig (1980), Variations in geologic structure along the Sunda forearc, Northeastern Indian Ocean, in *The Tectonic and Geologic Evolution of Southeast Asian Seas and Islands*, pp. 145–160, AGU, Washington, D. C.

Moore, G. F., et al. (2001), New insights into deformation and fluid flow processes in the Nankai Trough accretionary prism: Results of Ocean Drilling Program Leg 190, *Geochem. Geophys. Geosyst.*, *2*(10), 1058, doi:10.1029/2001GC000166.

Moore, G. F., et al. (2009), Structural and seismic stratigraphic framework of the NanTroSEIZE Stage 1 transect, in *Proc. IODP*, edited by M. Kinoshita et al., Integrated Ocean Drilling Program Management International Inc, Washington, D. C.

Moore, J. C., K. Moran, M. E. MacKay, and H. Tobin (1995), Frontal thrust, Oregon accretionary prism: Geometry, physical properties and fluid pressure, in *Proc. ODP, Sci. Results*, edited by B. Carson et al., Ocean Drilling Program, College Station, Tex.

Moore, J. C., C. Rowe, and F. Meneghini (2007), How accretionary prisms elucidate seismogenesis in subduction zones, in *The Seismogenic Zone of Subduction Thrust Faults*, edited by T. H. Dixon and J. C. Moore, pp. 288–315, Coumbia Univ. Press, New York.

Natawidjaja, D. H., K. Sieh, S. N. Ward, H. Cheng, R. L. Edwards, J. Galetzka, and B. W. Suwargadi (2004), Paleogeodetic records of seismic and aseismic subduction from central Sumatran microatolls, Indonesia, *J. Geophys. Res.*, *109*, B04306, doi:10.1029/2003JB002398.

Natawidjaja, D. H., K. Sieh, M. Chlieh, J. Galetzka, B. W. Suwargadi, H. Cheng, R. L. Edwards, J.-P. Avouac, and S. N. Ward (2006), Source parameters of the great Sumatran megathrust earthquakes of 1797 and 1833 inferred from coral microatolls, *J. Geophys. Res.*, *111*, B06403, doi:10.1029/2005JB004025.

Newcomb, K. R., and W. R. McCann (1987), Seismic history and seismotectonics of the Sunda Arc, *J. Geophys. Res.*, *92*(B1), 421–439, doi:10.1029/JB092iB01p00421.

Park, J.-O., T. Tsuru, S. Kodaira, P. R. Cummins, and Y. Kaneda (2002), Splay Fault Branching Along the Nankai Subduction Zone, *Science*, *297*(5584), 1157–1160.

Polonia, A., and L. Torelli (2007), Antarctic/Scotia plate convergence off southernmost Chile, *Geol. Acta*, *5*(4), 295–306.

Reed, D. L., E. A. Silver, J. E. Tagudin, T. H. Shipley, and P. Vrolijk (1990), Relations between mud volcanoes, thrust deformation, slope sedimentation, and gas hydrate, offshore north Panama, *Mar. Pet. Geol.*, *7*(1), 44–54.

Rowe, C. D., F. Meneghini, and J. C. Moore (2009), Fluid-rich damage zone of an ancient out-of-sequence thrust, Kodiak Islands, Alaska, *Tectonics*, *28*, TC1006, doi:10.1029/2007TC002126.

Saffer, D. M., and H. J. Tobin (2011), Hydrogeology and mechanics of subduction zone forearcs: Fluid flow and pore pressure, *Annu. Rev. Earth Planet. Sci.*, *39*(1), 157–186.

Scholz, C. H. (1998), Earthquakes and friction laws, *Nature*, *391*(6662), 37–42.

Scholz, C. H., and J. Campos (2012), The seismic coupling of subduction zones revisited, *J. Geophys. Res.*, *117*, B05310, doi:10.1029/2011JB009003.

Seely, D. R. (1977), The significance of landward vergence and oblique structural trends on trench inner slopes, in *Island Arcs, Deep Sea Trenches, and Back-arc Basins*, edited by M. P. Talwani and C. Walter, pp. 187–198, AGU, Washington, D. C.

Singh, S. C., N. Hananto, M. Mukti, H. Permana, Y. Djajadihardja, and H. Harjono (2011), Seismic images of the megathrust rupture during the 25th October 2010 Pagai earthquake, SW Sumatra: Frontal rupture and large tsunami, *Geophys. Res. Lett.*, *38*, L16313, doi:10.1029/2011GL048935.

Smith, G., L. McNeill, T. J. Henstock, and J. Bull (2012), The structure and fault activity of the Makran accretionary prism, *J. Geophys. Res.*, *117*, B07407, doi:10.1029/2012JB009312.

Smith, G. L., L. C. McNeill, K. Wang, J. He, and T. J. Henstock (2013), Thermal structure and megathrust seismogenic potential of the Makran subduction zone, *Geophys. Res. Lett.*, *40*, 1528–1533, doi:10.1002/grl.50374.

Smith, W. H. F., and D. T. Sandwell (1997), Global sea floor topography from satellite altimetry and ship depth soundings, *Science*, *277*(5334), 1956–1962.

Tilmann, F. J., T. J. Craig, I. Grevemeyer, B. Suwargadi, H. Kopp, and E. Flueh (2010), The updip seismic/aseismic transition of the Sumatra megathrust illuminated by aftershocks of the 2004 Aceh-Andaman and 2005 Nias events, *Geophys. J. Int.*, *181*(3), 1261–1274.

Ujiie, K., et al. (2013), Low coseismic shear stress on the Tohoku-Oki megathrust determined from laboratory experiments, *Science*, *342*(6163), 1211–1214.

Wang, K., and Y. Hu (2006), Accretionary prisms in subduction earthquake cycles: The theory of dynamic Coulomb wedge, *J. Geophys. Res.*, *111*, B06410, doi:10.1029/2005JB004094.

Wells, R. E., R. J. Blakely, Y. Sugiyama, D. W. Scholl, and P. A. Dinterman (2003), Basin-centered asperities in great subduction zone earthquakes: A link between slip, subsidence, and subduction erosion?, *J. Geophys. Res.*, *108*(B10), 2507, doi:10.1029/2002JB002072